PAPER

Extremely high-efficiency solar steam generation, robust and scalable photothermal evaporator based on ZIF-67@MXene/rGO decorated rock wool†

Riski Titian Ginting, [ID] *[ab] Hairus Abdullah, [ID] [c] Diana Alemin Barus[d] and Vivi Fauzia[e]

Emerging solar steam generation techniques utilizing solar energy are considered as promising for seawater desalination and wastewater purification. Herein, for the first-time, recycled rock wool (RW) waste is used as a 3-dimensional (3D) evaporator, decorated with a novel hierarchical structure of zeolitic imidazolate framework (ZIF-67), MXene and reduced graphene oxide (rGO) as the photothermal evaporator, termed ZIF-67@MXene/rGO (ZMG). This evaporator demonstrates good thermostability, pH stability and is mechanically robust without any detachment of the RW fibers. Based on the strong light absorption, improved wettability and microchannels that facilitate accelerated water transport through the fibers, the RW/ZMG evaporator – with sample height of 3.5 cm – has a remarkable evaporation rate of 3.81 kg m^{-2} h^{-1}, corresponding to a solar-thermal conversion efficiency of 153.7%, achieved under 1 sun illumination. The highly efficient solar evaporator was correlated to the cold evaporation from the sidewall surface gaining extra energy from the environment. It is important to note that the solar evaporation performance is almost two times higher that of a pristine RW sample and far superior to most reported in the literature that have a larger sample height (≥6 cm), so it could also reduce the loading mass of photothermal materials. Meanwhile, the evaporator was highly stable in 20 wt% NaCl under 1 sun illumination over 12 h continuous tests, able to maintain its evaporation rate of 3.55 kg m^{-2} h^{-1} with no salt accumulation observed, revealing the impressive long-term salt durability. Moreover, the large-scale evaporator was fabricated and tested under outdoor conditions for practicability evaluation, and demonstrates excellent salt ion rejection (99.8%), effective removal of azo and organic dyes, acidic/ alkaline solution, and oil-in-water emulsions. These findings suggest that the cost-effective RW based evaporator provides a new concept for high performance solar steam generation, salt-resistant and multimedia purification applications.

Introduction

The rapid urbanization and development of modern industry has led to a growing need for energy and fresh water. Currently, conventional technologies such as multi-stage flash evaporation, thermal distillation, ion exchange and reverse osmosis are commonly used for seawater desalination to help solve the worldwide challenge of supplying clean water.[1–4] However, due to the enormous consumption of electrical energy, high operating cost and complex installation, alternative methods such as solar steam generation have attracted extensive attention, with the advantage of utilizing abundant solar irradiation as the input energy, being cost-effective and with a low carbon footprint.[5–7] In general, the working principle of a solar steam generation system consists of: water adsorption for a continuous water supply; and photothermal absorber for converting sunlight into thermal energy, generating vapor, where the condensed water is collected as freshwater.[8–10] There are five main key factors for an ideal photothermal evaporator: (i) full spectral range of light absorption, (ii) heat localization, (iii) good wettability of porous structure, (iv) excellent chemical and mechanical stability, (iv) salt-resistant property to avoid accumulation of salt.[11,12] Although extensive progress has been made using several device structures, the low evaporation rate

[a]Department of Electrical Engineering, Universitas Prima Indonesia, Medan, Indonesia. E-mail: titiangt@unprimdn.ac.id; titian@nrelab.com

[b]Nanomaterials for Renewable Energy Laboratory (NRE Lab), CV. Inovasi Teknologi Nano, Medan, Indonesia

[c]Department of Industrial Engineering, Universitas Prima Indonesia, Medan, Indonesia

[d]Department of Physics, Faculty of Mathematics and Natural Sciences, Universitas Sumatera Utara, Medan, Indonesia

[e]Department of Physics, Faculty of Mathematics and Natural Sciences, Universitas Indonesia, Depok, Indonesia

† Electronic supplementary information (ESI) available. See DOI: https://doi.org/10.1039/d2ta09778h

(<2 kg m^{-2} h^{-1}) and salt accumulation cause severe degradation of the evaporation rate, thus limiting the photothermal evaporator performance.[13,14]

For the past few years, a great deal of effort towards photothermal absorber materials has been conducted, reducing the heat loss and improving the solar steam generation efficiency, namely: cellulose acetate-MXene,[15] cotton sheet-rGO,[16] melamine foam-rGO/cellulose nanocrystals,[17] polystyrene foam-Ni@SiO$_2$ NPs,[18] PDA/KH550/TiO$_2$-PPy membrane[19] and polydopamine decorated nickel–cobalt bimetal.[20] The main advantage of 3D-based photothermal material are adjustable sample height to reduce the top and sidewall evaporator surface temperature, thus convection and radiation losses could be minimized.[21] Additionally, the evaporator can gain extra energy from the environment and avoid thermal energy loss to the bulk water, which gives rise to high photothermal conversion efficiency $\geq 100\%$ beyond the theoretical upper limit.[22] Rock wool (RW) is a good thermal and sound insulator commonly used as building insulation, a substrate for horticulture crop plants and flame retardants, but large amounts of its solid waste cause serious environmental concern. To overcome this issue, recycling RW waste into functional materials for sustainable development could involve turning it into higher value products such as heavy metal-ion absorbents,[23] filter beds,[24] used for oil–water separation,[25] photocatalysis[26] and electromagnetic interference shielding.[27] Recent reports on RW decorated with thermally insulating polymers of Cl$^-$ doped poly(3,4-ethylenedioxythiophene) as the photothermal absorber, demonstrate relatively poor solar steam generation performance with evaporation rate and efficiency of 1.64 kg m^{-2} h^{-1} and $\sim 80\%$, respectively.[28] However, most 3D designs of evaporators so far, are limited reports on evaporation rate and salt fouling resistance performance in highly concentrated saline solution (≥ 20 wt% NaCl).[29] Therefore, designing a hierarchical structure of photothermal absorber materials with strong light absorption coupled with hydrophilic wettability and thermal management *via* cold evaporation to enhance solar steam generation, is highly essential to meet the demand of rapid seawater desalination and salt rejection properties.

Herein, RW waste was utilized for the first time as a thermally insulated substrate decorated with a novel hierarchical structure design of hybrid nanocomposites as the photothermal absorber, for high efficiency solar steam generation. The zeolitic imidazolate framework (ZIF-67), a subset of metal organic frameworks (MOFs), consists of a cobalt ion (Co^{2+}) and 2-methylimidazolate ligands, and has shown potential applications in CO$_2$ adsorption, heavy metal and dye adsorption, oil–water separation, catalysis, solar-cells, energy storage, gas separation and sensors.[30] ZIF-67 is a porous material with good optical absorption properties, high crystallinity and high surface area.[31,32] Therefore, combining porous ZIF-67 with highly hydrophilic 2D MXenes [33] and the excellent light-to-heat conversion of reduced graphene oxide (rGO), might effectively convert solar to thermal energy for water evaporation. Accordingly, the facile preparation of hierarchical ZIF-67@MXene/rGO (ZMG) structures decorated on RW fibers through freeze drying, was developed to improve light absorption, hydrophilic

wettability and microchannel fibers, for facilitating sufficient water transport to the upper layer and sidewall of the evaporation surface for stable evaporation of high brine concentrated water. For comparison, pristine RW, RW decorated rGO (RW/G) and MXene (RW/M) evaporators with various heights of 0.5, 1.5, 2.5 and 3.5 cm, were also fabricated to understand the influence of sample height in solar steam generation performance. As expected, the RW/ZMG sample with a height of 3.5 cm demonstrates remarkable evaporation rate and efficiency of 3.81 kg m^{-2} h^{-1} and 153.7%, respectively, under 1 sun illumination, which is higher than RW, RW/G and RW/M due to its strong light absorption and superhydrophilicity. In addition, the RW/ZMG evaporator demonstrates excellent stability for seawater desalination (20 wt% NaCl) over 12 h of continuous illumination of 1 sun, with superior salt ions rejection, and is also capable of processing purified organic dyes, domestic wastewater, and oily wastewater.

Materials and methods

Materials

RW waste was obtained from local hydroponics farming in Medan city. Non-exfoliated MXene and rGO powder were supplied by ITNANO, Medan, Indonesia. PVA (M_w: 90 000 g mol^{-1}), methylene blue, congo red and methyl orange were purchased from Aldrich, Singapore. CoCl$_2 \cdot$6H$_2$O (99%) was acquired from Smart Lab, Indonesia. 2-Methylimidazole, NaCl, MgCl$_2$, KCl, MgSO$_4$, NaHCO$_3$, and CaCl$_2$ were procured from Merck Chemicals, Indonesia, and used without further purification.

Preparation of ZIF-67@MXene/rGO hybrid nanocomposites

Non-exfoliated MXene and rGO of concentration 3 mg mL^{-1}, were each added into 50 mL deionized water, followed by ultrasound with tapered tips (Vibra Cell VCX750) at an amplitude of 35% for 1 h with 10 s on–off cycles. 0.45 g CoCl$_2 \cdot$6H$_2$O and 5.5 g imidazole were mixed separately in 25 mL deionized water. The solution was held at room temperature for 24 h without stirring. Subsequently, the solution was centrifuged at 6000 rpm for 15 min, washed with methanol three times, followed by freeze drying at a pressure of 2 Pa and temperature of -65 °C for 24 h.

Preparation of RW-based evaporator

PVA (5 wt%) added into rGO, MXene and rGO/MXene/ZIF-67 solution with a concentration of 5 mg mL^{-1}. The solution was heated at 85 °C for 2 h to fully dissolve the PVA. Subsequently, each solution was brush decorated twice onto the surface of RW of size 2×2 cm^2 (top surface) and various heights of 0.5, 1.5, 2.5 or 3.5 cm. The brush decorated RW-based sample was then oven dried at 80 °C for 12 h, prior for being used for characterization and as an evaporator.

Material characterization

The surface morphology of RW, RW-G, RW-M and RW-GMZ were characterized using scanning electron microscopy (SEM,

This journal is © The Royal Society of Chemistry 2023

J. Mater. Chem. A, 2023, **11**, 5296–5308 | **5297**

EVO MA 10, Zeiss). The optical properties of all evaporators were measured in wet conditions and microstructural properties were recorded using a Jenway 7315 and Bruker D8 Advance, respectively. Fourier-transform infrared (FTIR) and Raman spectra were obtained using an FTIR Cary 630 (Agilent) and LabRam spectrometer (LabRAM HR Evolution, Horiba Jobin Yvon) with a 532 nm laser. The surface chemical composition for RW, RW-G, RW-M and RW-GMZ was evaluated using (XPS, ESCALAB 250Xi, Thermo Fisher Scientific). The water contact angle was determined on a lab-made goniometer coupled with high-speed camera (ITNANO, Indonesia) and the average values were taken from 4 different positions for each sample. The ion concentration of Na, Mg, K, Ca, Pb, Cd, Zn and Al were collected by inductively coupled plasma-optical emission spectrometry (ICP-OES; Varian 715-ES) with an SPS 4 autosampler.

Solar steam generation test

The solar steam generation measurements were performed under 1 sun illumination (100 mW cm^{-2}) using a Xenon lamp solar simulator (Zolix Sirius SS150, class ABA) equipped with a standard AM 1.5 G filter, where the light intensity was continuously monitored using a solar power meter (SM206). The RW, RW-G, RW-M and RW/ZMG sample top surface areas of 2×2 cm^2 with height variation from 0.5 to 3.5 cm, are floated on a cylindrical glass container (200 mL) filled with deionized water. The measurement was recorded at an ambient temperature of 26 ± 2 °C and humidity ~50%. During the evaporation process, the mass change was monitored with an analytical balance (Mettler Toledo, Al204, accuracy $\pm$ 0.1 mg). The

temperature at the top and side surface were recorded by an IR camera (HikMicro B20). In addition, the solar-desalination performance proceeded using simulated seawater with concentrations of NaCl, $MgCl_2$, KCl, $MgSO_4$, $NaHCO_3$, and $CaCl_2$ of 26.5, 24, 0.73, 3.3, 0.2, and 1.1 g L^{-1}, respectively. To evaluate the oil-in-water emulsion evaporation performance, palm oil mill effluent (POME) was collected from a local palm oil mill in Medan, Indonesia. To investigate the solar desalination performance of the RW-GMZ evaporator, a prototype water purification device for simulating solar water purification was built. The RW-GMZ evaporator (6 cm^2) with height 3.5 cm was placed in a 300 mL crystallizing dish and covered in a transparent glass dome containing 200 mL of brine solution obtained from Cermin beach, North Sumatra, Indonesia (location coordinates: 3°38′04.9″N 99°01′20.8″E).

Results and discussion

The fabrication and design structure of the RW-based evaporator are presented in Fig. 1a, where RW waste serves as the support and water transport system for evaporation, meanwhile MXene/rGO and *in situ* synthesis of ZIF-67, act as the solar absorber. As in Fig. 1a, MXene and rGO were added to deionized water separately and mixed together under strong ultrasonic agitation to obtain a stable suspension. To further increase the ability of strong light absorption and simultaneously improve photothermal conversion efficiency, the formation of ZIF-67 decoration on the MXene/rGO surface was carried out by a simple one-step aqueous room temperature method. After

Fig. 1 (a) Schematic illustration of the design and fabrication process of functionalized RW waste as a solar steam generation device, and (b) SEM image of freeze-dried ZIF-67 modified MXene/rGO surface.

freeze drying, Fig. 1b shows the SEM image of the polyhedral structure of ZIF-67 which was uniformly attached on the MXene/rGO surface as shown in the hybrid structure. The detailed morphology of ZIF-67@MXene/rGO is shown in Fig. S1d.† The addition of PVA and the hybrid composite on RW, followed by freeze drying, shows a rougher RW microfiber surface for generating RW/ZMG, as shown in the inset of Fig. 1a. Besides, each rGO and MXene were prepared as RW/G and RW/M samples for solar steam generation performance comparison.

The SEM images of the RW-based evaporator are shown in Fig. 2. Pristine RW comprised of random arrangements of mineral-based fibers of diameter 2–10 μm (Fig. 2a). The diameter of RW fibers was slightly increased (Fig. 2b–d) after contact with the decorated hybrid composite solution. It can be clearly seen that the fiber was fully covered, creating a rougher surface with formation of self-organized wrinkled structures heterogeneously attached to the RW fibers, which further confirms the strong interaction of hydrogen bonds between rGO, MXene and ZIF-67 with the PVA matrix. For RW/ZMG, a compact layer of PVA with interconnecting network of ZMG on arrangement of RW bundle fibers could facilitate multiple light reflections,

which could be beneficial to improve solar absorption. The elemental mapping analysis shows the uniform distribution of Ti, Co and N (Fig. 1e–g), while C and O can seen in the ESI (Fig. S1†), revealing the presence MXene, ZIF-67 and rGO on the RW fibers. Fig. 2h shows the UV-Vis spectra of rGO with a strong absorption peak at 268 nm due to $\pi–\pi^*$ transitions of the C=C bonds.[34] The broad peaks of MXene from 200–450 nm indicates the large sized flakes of the highly stable MXene,[35] and the additional peak at 786 nm is from the inherent out-of-plane inter-band transition of MXene.[36] For ZIF-67, the broad peak centered at 596 nm originates from $^4A_2(F) \rightarrow ^4T_1(P)$ transitions of Co(II) ions.[37] Accordingly, the broad absorption of ZIF67@MXene/rGO composites and red shift of the MXene peak to 793 nm is due to the interaction between MXene, rGO and ZIF-67.

To further confirm the successful functionalization of RW, the pristine RW and developed hybrid composite were determined by XRD analysis. As shown in Fig. 2i, the XRD profile of the RW waste sample shows a broad amorphous peak at 19.32°, which originated from the Al_2O_3, CaO, MgO and SiO_2 phase.[23] In comparison with RW waste, the diffraction peaks of RW/ZMG possess characteristics peaks of 6.2°, 19.2°, 36.3°, 39.1°. 41.8°
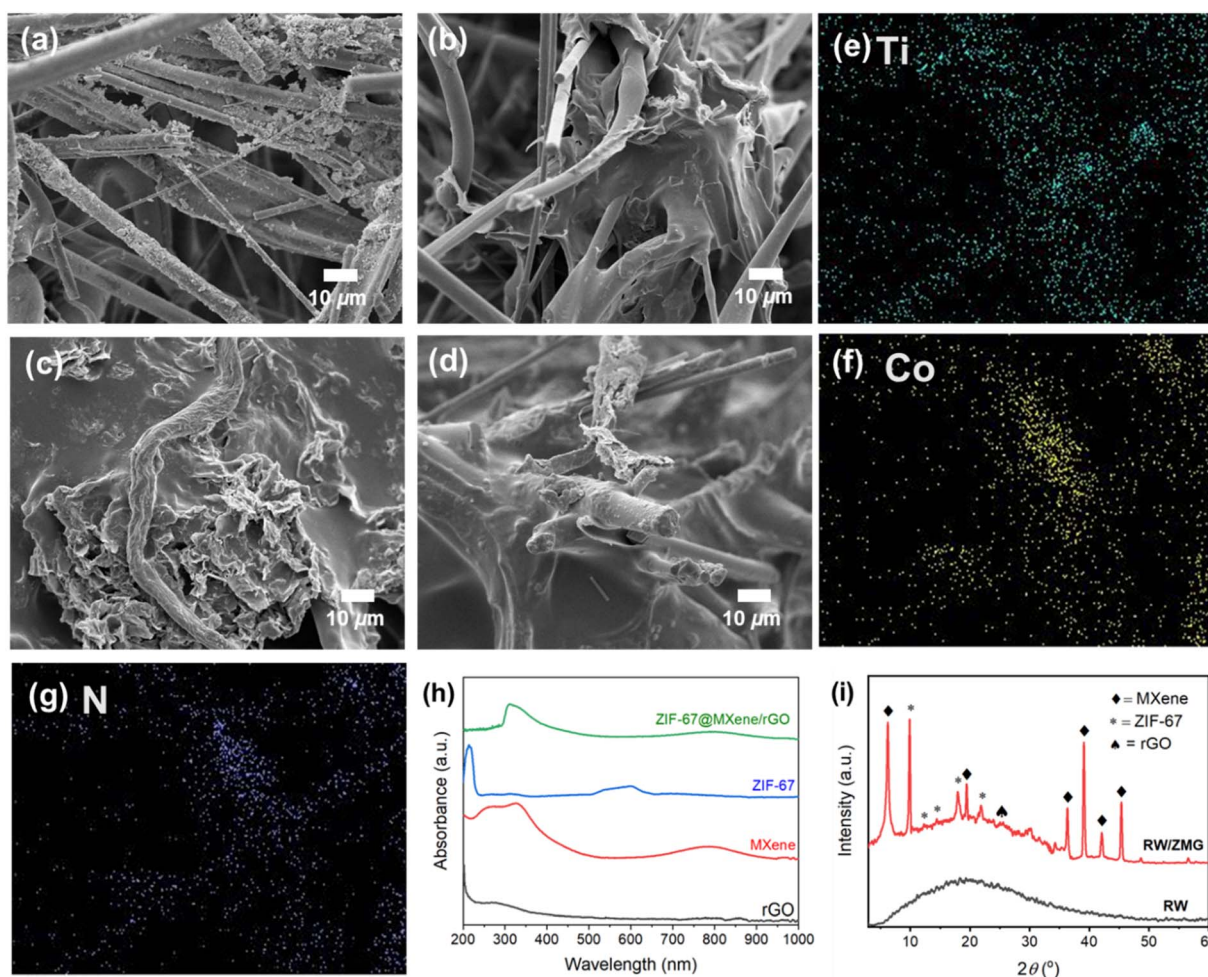

Fig. 2 SEM images of (a) RW waste, (b) RW/G, (c) RW/M, (d) RW/GMZ and its EDX mapping of (e) Ti, (f) Co and (g) N elements. (h) UV-Vis spectra of rGO, MXene, ZIF-67 and its composite. (i) XRD patterns of the RW-only and RW/ZMG samples.

This journal is © The Royal Society of Chemistry 2023

J. Mater. Chem. A, 2023, 11, 5296–5308 | 5299

and 45.3° assigned to (002), (004), (103), (104), (105) and (106) planes with low Ti_3AlC_2 impurities, due to incomplete etched MXene in the presence of Al.[38] It is worth noting that most literature reports (002) planes of MXene are located between 8 and 9°,[39,40] the shift of MXene (002) planes in the composite implies larger interlayer spacing of 1.42 nm, due to intercalation of rGO into MXene layers.[41,42] A small distinct peak at 25.0° is ascribed to the rGO, which proved the stability of the composite,[43] even after *in situ* synthesis of ZIF-67. Furthermore, strong peaks at 10.1°, 12.5°, 14.6° and 18.0° corresponding to (002), (112), (022) and (222) planes of highly crystalline ZIF-67 are consistent with previous reports of high crystallinity.[44,45] Moreover, the characteristics peak of ZIF-67 in the composite does not change in comparison with other literature[44] for pristine ZIF-67, thus the hybrid composite on RW fibers was prepared successfully. In addition, FTIR analysis (Fig. S1c†) revealed the peak shift from 3309 to 3280 cm^{-1}, which demonstrates the formation of a hydroxyl group between RW with PVA-ZMG.

In order to qualitatively demonstrate the RW-based evaporator light absorption, the absorption spectra were measured using UV-visible spectra of transmittance and reflectance as shown in Fig. 3a. As expected, the RW/ZMG sample exhibits the strongest light absorption of 96%, which is much higher than for RW/M, RW/G and pristine RW waste at 91, 87 and 33% across the UV-Vis-NIR, respectively. The large improvement of optical absorption of RW/ZMG is associated with the presence of ZIF-67. The physical characterization of pristine and functionalized RW were carried out using Raman spectroscopy.

Fig. 3b depicts the RW waste characteristic peaks between 800–1800 cm^{-1}, attributed to the non-bridging oxygen,[46] and bridging oxygen linkage of Si–O–Si and Al–O–Si from CaO–MgO–Al_2O_3–SiO_2 glass ceramics.[47] For the RW/ZMG sample, the weak Raman shift peak at 148 cm^{-1} (E_g^1 mode) correlates to the PVA matrix interrupting the in-plane vibrations of Ti_2 and C atoms.[48] Moreover, the peaks at 198 and 274 cm^{-1} related to the A_{1g} out of plane MXene are due to the incomplete removal of Al,[49,50] which is consistent with the XRD result in Fig. 2i, and is commonly observed for MXene treated with HCl and LiF.[51] The other Raman shift of the peak at 430 cm^{-1} correlates with the functional surface species (T_x) of MXene.[50] The prominent peak located at 698 cm^{-1} can be assigned to Co ions[52] and Co_3N (metal–N bond) of ZIF-67.[53] In addition, the Raman scattering peaks at 1350 cm^{-1} (D band) and 1590 cm^{-1} (G band) of RW/ZMG can be observed with an I_D/I_G ratio of 1.17, which further confirmed the graphitic structure of rGO.[54] Besides, the high I_D/I_G ratio further proves the strong interaction between rGO with the ZIF-67@MXene composite.

To further confirm the elemental composition and surface electronic states of ZIF-67@MXene/rGO attached on RW fibers, we used XPS analysis. From the XPS survey, Ti, C, Co, N and O elements were clearly detected as shown in Fig. 3c, which is consistent with the EDX results. Fig. 3d shows the peak at 455.3 and 461.5 eV can be ascribed to Ti $2p_{3/2}$ and Ti $2p_{1/2}$, with spin–orbit splitting, ΔTi_{2p}, of 6.2 eV, thus correlating to the Ti–C bond of MXene.[55,56] The presence of the Ti–C bond in high resolution Ti 2p revealed the stability of MXene. Interestingly, there is no Ti–O peak observed which indicates that the MXene
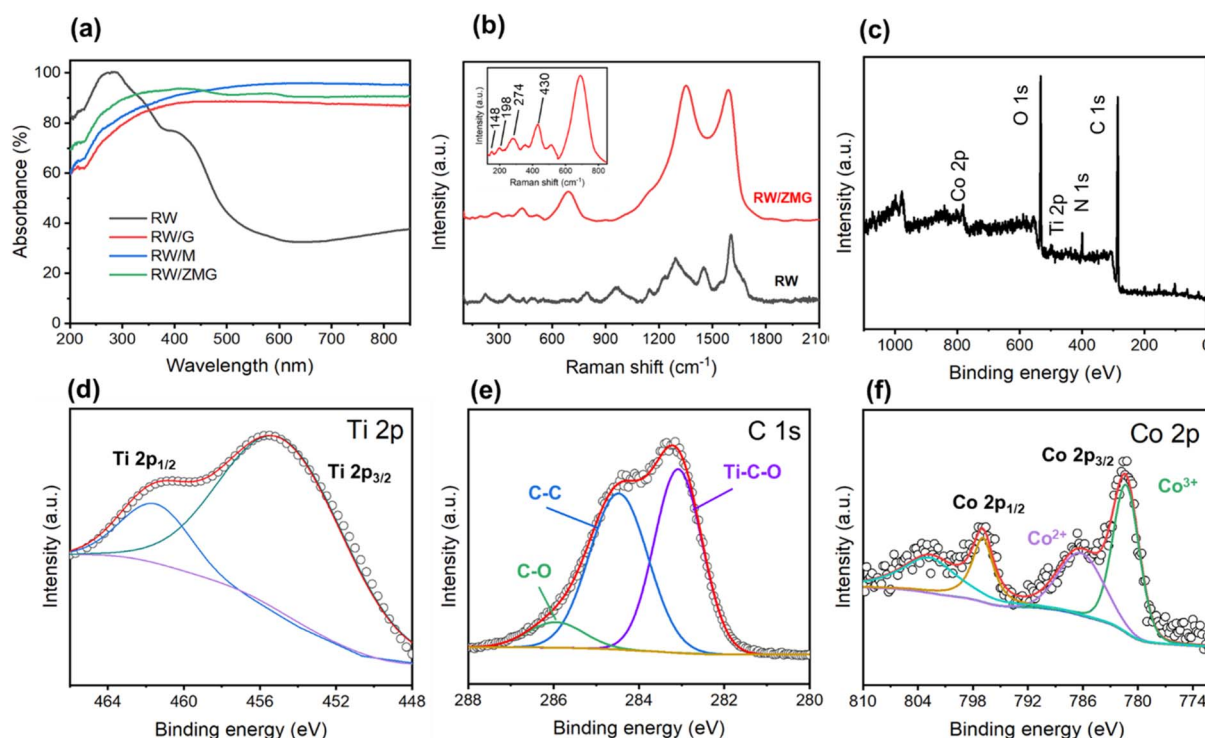

Fig. 3 (a) Absorption spectra and (b) Raman spectra of the RW-based evaporator. Inset shows the MXene Raman peaks. (c) Survey spectrum and high resolution XPS spectrum of (c) C 1s, (d) Ti 2p, (e) Co 2p and (f) N 1s, from the RW/ZMG sample.

5300 | *J. Mater. Chem. A*, 2023, **11**, 5296–5308

This journal is © The Royal Society of Chemistry 2023

oxidation was hindered during synthesis of ZIF-67. Fig. 3e shows high resolution XPS of the C 1 s spectrum with three distinct peaks at 283.1, 284.5 and 285.9 eV, assigned to the Ti–C–O, C–C and C–O bonds, respectively, which is in good agreement with a previous report.[57] Fig. 3f shows peaks at 781.4 and 797.1 eV, corresponding to the Co $2p_{3/2}$ for Co^{3+} and its satellite peaks, contributed by the Co $2p_{1/2}$ of Co^{2+}.[58,59] For the O 1s XPS spectrum (Fig. S2a†), the deconvoluted peaks at 531.3, 532.0, and 533.2 eV could be assigned to $C–Ti–O_x$, $C–Ti–OH_x$ and surface adsorbed oxygen.[55] Additionally, the N 1s deconvoluted peak (Fig. S2b†) centered at 398.9 and 400.4 eV belong to the pyridinic and pyrrolic-N from 2-MIM,[60] respectively, which verify the presence of the Co–N bond of the ZIF-67@MXene/rGO composite on RW fibers.

In order to understand the stability of the RW/ZMG sample under extreme conditions – strong ultrasonic agitation for 2 h

(power of 200 W), heating at 90 °C for 2 h, immersion in pH ∼ 1 or 14 solutions for 24 h, followed by a compression–release cycle 20 times – were carried out as seen in Fig. 4a. It can be clearly observed that there is no residual or detachment of the fibers based on the microscopic images (Fig. S3†) due to improved adhesion between ZIF-67@MXene/rGO and RW with the addition of PVA. This finding reveals the superior durability and structural stability in comparison to pristine RW waste, which undergoes rapid structural disintegration (presence of voids) after immersion in acidic/alkaline pH and compression–release tests, as shown in Fig. S3.† The surface wettability properties of the pristine and functionalized RW waste were evaluated quantitatively by contact angle measurements from the surface by averaging 5 different samples. Fig. 4b shows the contact angle change with time evolution, and it can be clearly observed that RW demonstrates 88.31 ± 0.47° after the water droplet
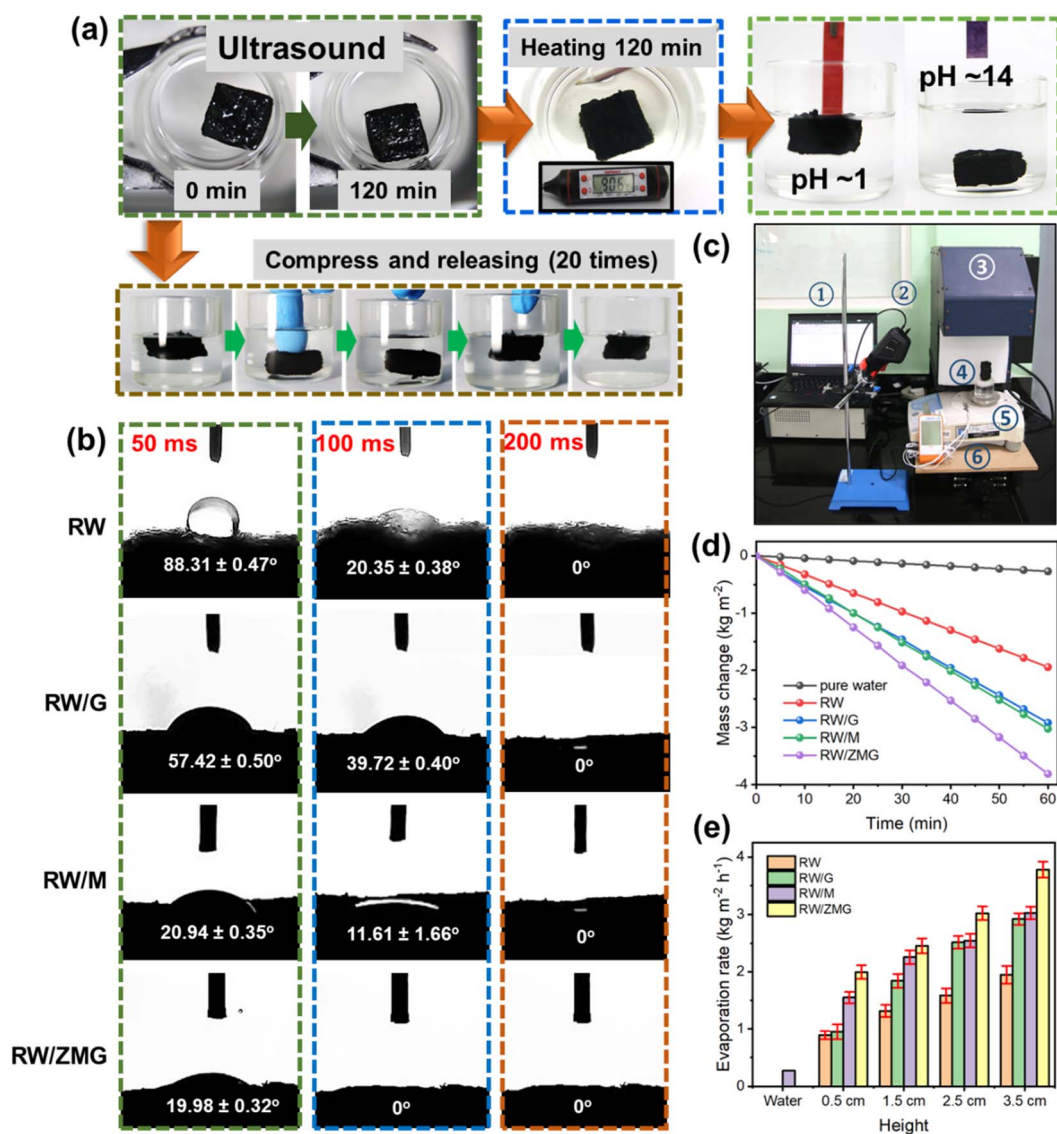

Fig. 4 (a) Photograph of RW/ZMG samples in durability and stability tests under severe conditions; (b) time-lapse capture of water droplet for the different evaporators; (c) photograph of solar steam generation setup, (1) laptop, (2) thermal camera, (3) solar simulator with AM1.5 G filter, (4) evaporator, (5) analytical balance and (6) humidity monitor; (d) time-dependent mass change of water for the RW-based evaporators with height 3.5 cm; and (e) evaporation rate under illumination of 100 mW cm^{-2} (1 sun) with the RW-based evaporators of different heights.

This journal is © The Royal Society of Chemistry 2023

J. Mater. Chem. A, 2023, **11**, 5296–5308 | **5301**

reaches the surface of the RW fibers at 50 ms. Subsequently after 100 and 200 ms, the contact angle reduces to $20.35 \pm 0.38°$ and $0°$, respectively. In contrast, the RW/G sample shows a higher contact angle of $39.72 \pm 0.40°$ at 100 ms owing to the hydrophobic nature of rGO.[61] The contact angle of the RW/M and RW/ZMG samples at 100 ms, recede to $11.61 \pm 1.66°$ and $0°$, respectively, due to the superhydrophilic properties facilitated by the mesoporous structure of MXene and ZIF-67@MXene, thus being advantageous for water transport as compared to the RW-waste sample. Most importantly, the significant improvement of RW/ZMG wettability could promote better solar steam performance. The solar steam performance of the RW-based evaporator was determined under the laboratory setup using a solar simulator (Fig. 4c). Fig. 4d depicts the mass change of water as a function of time under 1 sun illumination for a 3.5 cm sample height, meanwhile the mass changes with various heights and under dark conditions as shown in Fig. S4 and S5,† respectively. As demonstrated in Fig. 4d, the evaporation rates of RW, RW/G, RW/M and RW/ZMG with height 3.5 cm, were 1.94, 2.92, 3.02 and 3.81 kg m^{-2} h^{-1}, respectively, which is significantly higher than pure water of 0.27 kg m^{-2} h^{-1} under the same illumination. According to Fig. 4e, the increment of evaporation rate for the RW-based evaporators is consistent with the increase of evaporator height and the details are summarized in Table S1.† As

expected, the RW/ZMG evaporator shows the highest evaporation rate of almost 2 times and 14 times higher than pristine RW and pure water, respectively. Nevertheless, the dark evaporation rate of all evaporators with a similar height of 3.5 cm, is $\sim$1.50 kg m^{-2} h^{-1}, thus further confirming that evaporation in the dark does not contribute to the enhancement of evaporation rate under light for RW/G, RW/M and RW/ZMG.

In order to evaluate the reason behind the significant improvement of RW/ZMG evaporation rate, the IR temperature data of the top and side surface of all evaporators were recorded as shown in Fig. 5a. It can be clearly seen that after exposure to 1 sun illumination for 30 min, the top surface rapidly increased from room temperature to reach a maximum temperature of 35.0, 31.9, 35.8 and 33.9 °C for RW, RW/G, RW/M and RW/ZMG, respectively. The temperature changes as a function of time between the top and sidewall surfaces with various heights of all samples shown in Fig. S6 and S7,† respectively. Fig. 5b summarizes the top and side maximum surface temperature for RW, RW/G, RW/M and RW/ZMG samples of various height. It is found that both the top and side surface temperature decreases with increased height for all RW-based evaporators, which is in good agreement with previous reports.[15,20] For the RW waste evaporator, the top and side surface temperature were higher than the environmental temperature, which suggests high energy loss to the environment through radiation and
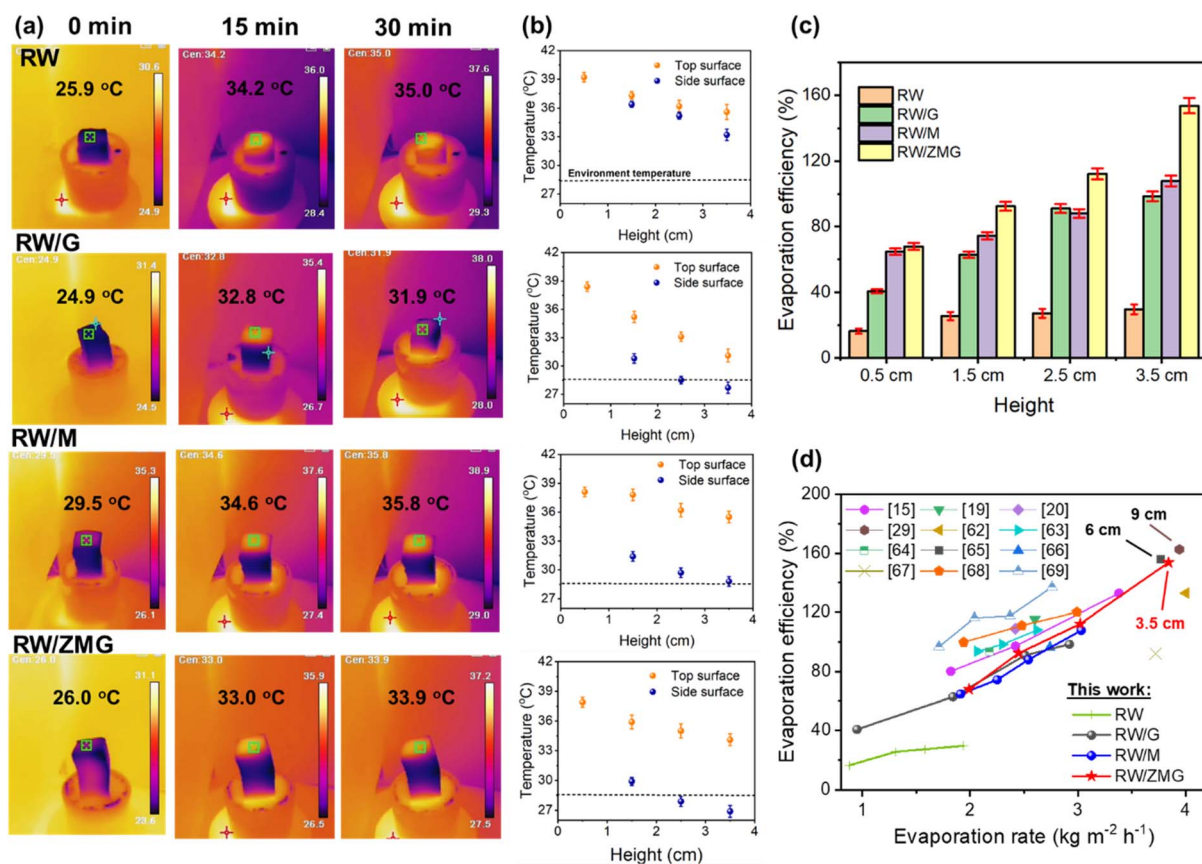

Fig. 5 (a) IR thermal images profile (evaporator height 3.5 cm) under illumination of 1 sun and the corresponding top surface temperature, (b) top and side surface temperature of the evaporators, (c) evaporation efficiency against evaporator height and (d) the comparison of evaporation efficiency and rate between the RW-based evaporator and previously reported evaporators with a similar height under 1 sun illumination.

5302 | *J. Mater. Chem. A*, 2023, **11**, 5296–5308

This journal is © The Royal Society of Chemistry 2023

convection, which increases with height from 0.5 to 3.5 cm. However, the RW/ZMG evaporator demonstrates a lower side temperature (26.8 °C) than environmental temperature (28.5 °C), hence the large difference in temperature between the top and side surface, leading to more energy gain from the ambient environment. Based on the temperature data, the solar–thermal energy conversion efficiency (η) can be calculated using the following equations:[62]

$$\eta = m(H_{Lv} + Q)/E_{in} \tag{1}$$

$$H_{Lv} = 1.91846 \times 10^6 [T_1/(T_1 - 33.91)]^2 \tag{2}$$

$$Q = c(T_1 - T_0) \tag{3}$$

where m is the net evaporation rate (kg m^{-2} h^{-1}), H_{Lv} is the latent heat of water vaporization (J kg^{-1}), T_1 is the stable maximum temperature reached by the top surface evaporator (°C), Q is the sensible heat of water (J kg^{-1}), c is the specific heat of water (4.2 J g^{-1} K^{-1}), T_0 is the initial temperature of the top surface of the evaporator (°C) and E_{in} is the energy input of light illumination (1 sun = 3600 kJ m^{-2} h^{-1}). The calculated evaporation efficiency is summarized in Fig. 5c and Table S1† under 1 sun illumination. In a similar trend to evaporation rate, the evaporation efficiency increases with height for all samples and reaches the highest efficiency, at 3.5 cm for RW, RW/G, RW/M and RW/ZMG, of 29.7, 98.5, 107.9 and 153.7%, respectively. Fig. 5d shows the evaporation efficiency against evaporation rate compared with previous literature reports.[15,63,64] There are some similar performances with other evaporators,[65-69] but the sample heights used in these was much higher (>6 cm) than the current work on RW/ZMG (3.5 cm). The detailed comparison can be refer to Table S2.† The outstanding solar steam performance of the RW/ZMG evaporator is not only due to multiple reflections by the bundle fibers with enhanced light absorption, but also the high evaporation rate of 1.5 kg m^{-2} h^{-1} under dark conditions.

To better understand the superior solar steam performance of RW/ZMG, the net energy gained from the environment (E_{enviro}) can be estimated based on the following equation:[16]

$$E_{enviro} = -A_1 \varepsilon \sigma (T1^4 - TE^4) - A_2 \varepsilon \sigma (T_2^4 - T_E^4) - A_1 h (T_1 - T_E) - A_2 h (T_2 - T_E) - q_{water} \tag{4}$$

$$q_{water} = cM\Delta T/t \tag{5}$$

where A_1 and A_2 are the top (4 cm^2) and sidewall area of the evaporator area (12, 20 and 28 cm^2 for heights 1.5, 2.5 and 3.5 cm, respectively). T_1, T_2, and T_E are the temperature of the top (4 cm^2) and side surface of the evaporator, and environmental temperature (°C). ε is the emissivity of the evaporation surface (~0.90), h is the convection heat transfer coefficient (assumed to be 10 W m^{-2} K^{-1}); q_{water} is the amount of heat gain by the evaporator from bulk water (W), where M is the weight of bulk water (200 g), ΔT is the temperature difference before and after 1 sun illumination (0.4 °C) for water and t is the time for energy transfer from water to evaporator (3600 s).[29] The calculated net energy gain is dependent on height variation for all

samples, refer to Table S1.† Hence, the total net energy of RW is −0.158 W (height 3.5 cm), therefore the evaporator loses its energy to the surrounding environment (negative value) as evidenced by the sidewall temperature higher than the environment, leading to low evaporation rate and efficiency (<40%) as shown in Fig. 5c. On the other hand, the net energy gain for RW/G, RW/M and RW/ZMG is 0.11, 0.05 and 0.128 W (positive value), respectively, for samples of height 3.5 cm. In addition, the total net energy gain of RW/ZMG is one order of magnitude with a total energy input of 1 sun illumination of ~0.4 W (top surface). This result suggests that the net energy gain from the environment could be enhanced with the composite of ZIF-67@MXene/rGO due to cold evaporation (lower than the environment temperature) through the evaporator sidewall (Fig. 5b), hence higher evaporation rate and efficiency was achieved. The possible mechanism of cold evaporation was due to temperature gradients, where the heat conduction from the top evaporation surface and bulk water were transferred to the sidewall surface without any radiation loss, thus gain energy from the environment.[22]

The evaporation rate under simulated seawater and acidic/alkaline pH conditions were carried out to understand the durability of the RW/ZMG evaporator. Fig. 6a shows the mass change against evaporation time, and the data are summarized in Fig. S8a.† Negligible changes are observed for evaporation rate with simulated seawater, meanwhile under acidic or alkaline solution, the evaporation rate only slightly decreased. Moreover, RW/ZMG could deliver stable neutral pH collected from condensed water (Fig. S8b†), which implies that the evaporator could cover a wide range of wastewater. Fig. 6b depicts the time-dependent mass change of water containing brine salinity of 3.5, 7, 15 and 20 wt% NaCl solution, resulting in an evaporation rate of 3.72, 3.70, 3.40 and 3.55 kg m^{-2} h^{-1} (Fig. 6c). Notably, the slight decrease can be explained due to the large surface tension between the evaporator surface and brine solution compared to pure water.[70] Fig. 6d presents the stability test of the RW/ZMG evaporator in brine salinity of 20 wt% NaCl solution, without any changes in evaporation rate up to 12 h of continuous tests under 1 sun illumination. As a result, steam generation performance was clearly highly stable without any accumulation of crystal salt observed on the evaporator surface (Fig. S9a and b†), thus confirming the impressive long-term salt durability and promising application for seawater desalination with antifouling properties. To further determine the salt resistance performance, 0.5 g of salt were loaded on top of the RW/ZMG evaporator surface floated on 20 wt% NaCl solution, as illustrated in Fig. 6e. After the evaporator was exposed to 1 sun illumination for 45 min, the salt crystals gradually dissipated on top of the surface. This rapid salt rejection proves the regeneration ability of the RW/ZMG evaporator and is beneficial for representing real conditions during day and nighttime cycles. Accordingly, the salt rejection mechanism of the RW/ZMG evaporator can be explained as illustrated in Fig. 6f. The combined mesopores[23] and micro-channel structures[71] of RW could accelerates brine water adsorption through interconnecting microfibers decorated with hierarchical ZIF-67@MXene/rGO structures. The detailed

Fig. 6 (a) The mass change of simulated seawater at various pH and (b) salt concentration, over time. (c) The evaporation rate of the RW/ZMG evaporator (3.5 cm) as a function of salt concentration (the inset photos show RW/ZMG in pure water and 20 wt% NaCl). (d) The cycling tests of solar steam generation using the RW/ZMG evaporator (height 3.5 cm) in brine solution 20 wt% NaCl under 1 sun illumination. (e) Self-regenerating and salt-resistance performance of RW/ZMG kept under ambient conditions. (f) Schematic diagram shows the working principle of the RW/ZMG evaporator.

wetting process was demonstrated in Fig. S9c,† which clearly indicates the rapid water transport of the RW/ZMG evaporator. Subsequently, it gives rise to capillary forces for sufficient water flux in the vertical direction from bulk brine water to the high salt concentration on the upper part of the evaporator. This causes a salt concentration gradient, thus leading to the immediate exchange to lower salinity *via* diffusion (salinity exchange), where salt ions are gradually diluted and transported to the bulk brine solution.[5,72–74] Furthermore, the advantageous RW/ZMG superhydrophilicity could prevent salt formation on both the top and sidewall of the evaporator surface, boosting the vaporization of brine water.

To determine the practicability of the RW/ZMG evaporator in solar desalination, a simple prototype system placed in outdoor environment with real seawater and carried out for evaporation from 11 : 00 to 18 : 00 under average solar illumination of 390 mW cm^{-2} as shown in Fig. 7a. As displayed in Fig. 7b, the device was deployed on the roof of NRE Lab (CV. Inovasi Teknologi Nano, Medan) with total collected purified water weight about 5.2 L m^{-2} day^{-1} with large area RW/ZMG evaporator of 36 cm^2. The top surface and internal temperature of RW/ZMG was increased and decreased depending on the outdoor solar irradiation as shown in Fig. S10a,† which is in good agreement with experimental result. Fig. 7c depicts the desalinated water collected from the prototype system with four primary ions of Na$^+$, K$^+$, Ca^{2+} and Mg^{2+} of 9.68, 2.95, 2.82 and 1.41 mg L^{-1}, respectively were reduced by three order magnitude and much lower than WHO and EPA standard for drinking water, where the ion rejection of 99.8% was achieved. Besides, the heavy metal contamination obtained from domestic wastewater such
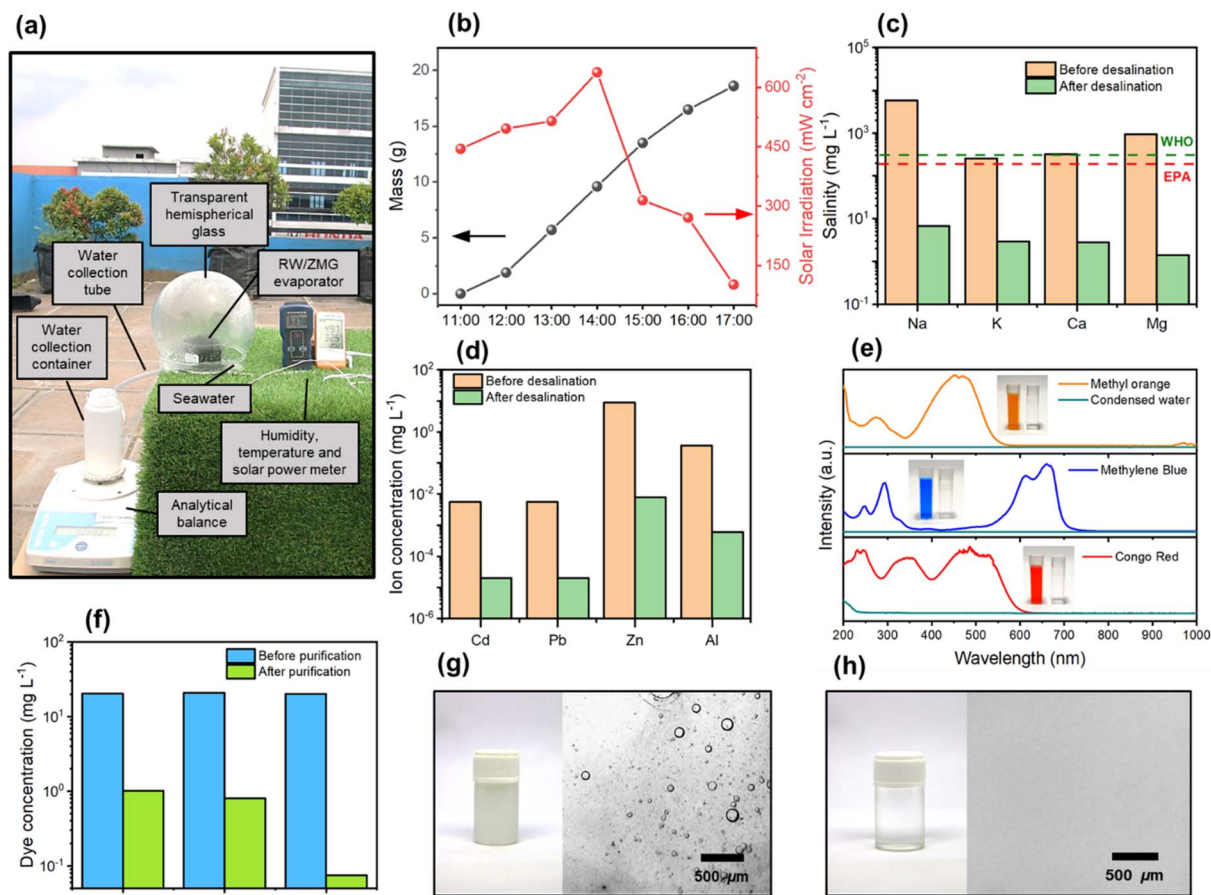
5304 | *J. Mater. Chem. A*, 2023, **11**, 5296–5308

This journal is © The Royal Society of Chemistry 2023

Fig. 7 (a) Photograph of outdoor water evaporation experiment prototypes with sealed dome-type chambers, (b) mass of water collected on evaporator (6 × 6 cm^2) under natural sunlight. (c) The concentration of four kind of primary ions (Na$^+$, K$^+$, Ca^{2+} and Mg^{2+}), (d) heavy metal ions (Cd^{2+}, Pb^{2+}, Zn^{2+} and Al^{3+}) of before and after desalination from domestic wastewater, (e) UV-Vis spectra of MO, MB and CR organic dyes solution and (f) removal performance before and after purification. (g) Micrographs and optical microscope photos of oil/water emulsion before and (h) after purification.

as Cd, Pb, Zn and Al ions were significantly reduced by 99.9% as shown in Fig. 7d. Moreover, the removal of congo red (CR), methylene blue (MB) and methyl orange (MO) solution were evaluated using RW/ZMG evaporator under 1 sun illumination. From Fig. 7e, the strong absorption peaks of organic dyes CR, MB and MO are 458, 660 and 484 nm, respectively with concentration of 20 mg L^{-1}. The collected condensed water demonstrate that organic dyes was completely remove >95% (transparent solution, inset Fig. 7e) with concentration of 1.07, 0.79 and 0.07 mg L^{-1} for CR, MB and MO, respectively as shown in Fig. 7f. The oil-in-water emulsion was also tested using RW/ZMG evaporator under 1 sun illumination and the mass change against time was depicted in Fig. S10.† The evaporation rate is as high as 3.66 kg m^{-2} h^{-1} slightly lower than evaporation rate of pure water (Table S1†) could be due to accumulation of oil droplet hindering the efficient water adsorption by evaporator. Fig. 7g and h displayed the optical microscope image of before and after purification, where the solution of oil-in-water emulsion was turbid and droplet could turn into clear water solution without any evidence of droplet was observed.

Conclusions

In summary, the hierarchical structure of ZIF-67@MXene/rGO hybrid nanocomposites decorated on RW waste, with the addition of PVA as a highly efficient photothermal evaporator, was successfully developed as confirmed by Raman and XPS analysis. The RW/ZMG evaporator demonstrates strong light absorption and superhydrophilicity suitable for solar steam generation. The combination of these merits results in an extremely high evaporation rate of 3.81 kg m^{-2} h^{-1} and evaporation efficiency of 153.7% under 1 sun illumination for a RW/ZMG evaporator with a sample height of 3.5 cm as compared with RW, RW/G and RW/M evaporators. The RW/ZMG evaporator demonstrates significantly higher performance than most previously reported literature at similar sample height. The enhanced performance is not only due to the simultaneous effect of multiple reflections by the RW fibers leading to light trapping and superhydrophilicity, but also cold evaporation of the sidewall surface by gaining energy from the environment. In addition, the RW/ZMG evaporator was highly stable for 12 h of

continuous tests under 1 sun illumination in brine salinity of 20 wt% NaCl solution, implying the durability and promising application for seawater desalination, with salt ions rejection of 99.8%. Most importantly, this finding illustrates that the RW/ZMG evaporator demonstrated great robustness, remarkable chemical resistance (acidic and alkaline), and multimedia purification (organic dyes, wastewater, and oil-in-water emulsion). Therefore, the simple and low-cost strategy utilizing RW waste with hybrid nanocomposites as the photothermal absorber, provides a new pathway towards scalable and efficient solar steam generation for solving water shortage issues.

Conflicts of interest

There are no conflicts to declare.

Acknowledgements

References

1 N. Ghaffour, T. M. Missimer and G. L. Amy, Technical review and evaluation of the economics of water desalination: current and future challenges for better water supply sustainability, *Desalination*, 2013, **309**, 197–207.

2 Y. Fan, S. Chen, H. Zhao and Y. Liu, Distillation membrane constructed by TiO_2 nanofiber followed by fluorination for excellent water desalination performance, *Desalination*, 2017, **405**, 51–58.

3 H. Li and L. Zou, Ion-exchange membrane capacitive deionization: a new strategy for brackish water desalination, *Desalination*, 2011, **275**, 62–66.

4 M. Qasim, M. Badrelzaman, N. N. Darwish, N. A. Darwish and N. Hilal, Reverse osmosis desalination: a state-of-the-art review, *Desalination*, 2019, **459**, 59–104.

5 C. Liu, K. Hong, X. Sun, A. Natan, P. Luan, Y. Yang and H. Zhu, An 'antifouling' porous loofah sponge with internal microchannels as solar absorbers and water pumpers for thermal desalination, *J. Mater. Chem. A*, 2020, **8**, 12323–12333.

6 H. Geng, Q. Xu, M. Wu, H. Ma, P. Zhang, T. Gao, L. Qu, T. Ma and C. Li, Plant leaves inspired sunlight-driven purifier for high-efficiency clean water production, *Nat. Commun.*, 2019, **10**, 1–10.

7 J. Xiao, Y. Guo, W. Luo, D. Wang, S. Zhong, Y. Yue, C. Han, R. Lv, J. Feng and J. Wang, A scalable, cost-effective and salt-rejecting MoS2/SA@melamine foam for continuous solar steam generation, *Nano Energy*, 2021, **87**, 106213.

8 R. T. Ginting, H. Abdullah and V. Fauzia, Facile preparation of MXene and protonated-g-C_3N_4 on natural latex foam for highly efficient solar steam generation, *Mater. Lett.*, 2022, **313**, 131779.

9 R. T. Ginting, H. Abdullah, E. Taer, O. Purba and D. Perangin-angin, Novel strategy of highly efficient solar-driven water evaporation using MWCNTs-ZrO_2-Ni@CQDs composites as photothermal materials, *Colloids Surf., A*, 2022, **642**, 128653.

10 K. S. Lau, R. T. Ginting, S. T. Tan, S. X. Chin, S. Zakaria and C. H. Chia, Sodium cholate as efficient green reducing agent for graphene oxide *via* flow reaction for flexible supercapacitor electrodes, *J. Mater. Sci.: Mater. Electron.*, 2019, **30**, 19182–19188.

11 G. Ni, G. Li, S. V. Boriskina, H. Li, W. Yang, T. Zhang and G. Chen, Steam generation under one sun enabled by a floating structure with thermal concentration, *Nat. Energy*, 2016, **1**, 1–7.

12 L. Shi, X. Wang, Y. Hu, Y. He and Y. Yan, Solar-thermal conversion and steam generation: a review, *Appl. Therm. Eng.*, 2020, **179**, 115691.

13 X. Wu, Y. Wang, P. Wu, J. Zhao, Y. Lu, X. Yang and H. Xu, Dual-zone photothermal evaporator for antisalt accumulation and highly efficient solar steam generation, *Adv. Funct. Mater.*, 2021, **31**, 2102618.

14 T. T. Pham, T. H. Nguyen, T. A. H. Nguyen, D. D. Pham, D. C. Nguyen, D. B. Do, H. V. Nguyen, M. H. Ha and Z. H. Nguyen, Durable, scalable and affordable iron(III) based coconut husk photothermal material for highly efficient solar steam generation, *Desalination*, 2021, **518**, 115280.

15 W. Li, X. Tian, X. Li, J. Liu, C. Li, X. Feng, C. Shu and Z.-Z. Yu, An environmental energy-enhanced solar steam evaporator derived from MXene-decorated cellulose acetate cigarette filter with ultrahigh solar steam generation efficiency, *J. Colloid Interface Sci.*, 2022, **606**, 748–757.

16 T. Gao, X. Wu, Y. Wang, G. Owens and H. Xu, A hollow and compressible 3D photothermal evaporator for highly efficient solar steam generation without energy loss, *Solar RRL*, 2021, **5**, 2100053.

17 H. Li, D. Jia, M. Ding, L. Zhou, K. Wang, J. Liu, C.-Y. Liu and C. Li, Robust 3D graphene/cellulose nanocrystals hybrid lamella network for stable and highly efficient solar desalination, *Solar RRL*, 2021, **5**, 2100317.

18 D. Ding, H. Wu, X. He, F. Yang, C. Gao, Y. Yin and S. Ding, A metal nanoparticle assembly with broadband absorption and suppressed thermal radiation for enhanced solar steam generation, *J. Mater. Chem. A*, 2021, **9**, 11241–11247.

19 C. Wei, X. Zhang, S. Ma, C. Zhang, Y. Li, D. Chen, H. Jiang, Z. Xu and X. Huang, Ultra-robust vertically aligned three-dimensional (3D) Janus hollow fiber membranes for interfacial solar-driven steam generation with salt-resistant and multi-media purification, *Chem. Eng. J.*, 2021, **425**, 130118.

20 B. Shao, Y. Wang, X. Wu, Y. Lu, X. Yang, G. Y. Chen, G. Owens and H. Xu, Stackable nickel–cobalt@polydopamine nanosheet based photothermal sponges for highly efficient solar steam generation, *J. Mater. Chem. A*, 2020, **8**, 11665–11673.

21 X. Wu, Z. Wu, Y. Wang, T. Gao, Q. Li and H. Xu, All-cold evaporation under one sun with zero energy loss by using

5306 | *J. Mater. Chem. A*, 2023, **11**, 5296–5308

This journal is © The Royal Society of Chemistry 2023

a heatsink inspired solar evaporator, *Adv. Sci.*, 2021, **8**, 2002501.

22 H. Song, Y. Liu, Z. Liu, M. H. Singer, C. Li, A. R. Cheney, D. Ji, L. Zhou, N. Zhang and X. Zeng, Cold vapor generation beyond the input solar energy limit, *Adv. Sci.*, 2018, **5**, 1800222.

23 L. Zhou, R. Li, G. Zhang, D. Wang, D. Cai and Z. Wu, Zero-valent iron nanoparticles supported by functionalized waste rock wool for efficient removal of hexavalent chromium, *Chem. Eng. J.*, 2018, **339**, 85–96.

24 A. Wanko, J. Laurent, P. Bois, R. Mosé, C. Wagner-Kocher, N. Bahlouli, S. Tiffay, B. Braun and P.-W. Provo kluit, Assessment of rock wool as support material for on-site sanitation: hydrodynamic and mechanical characterization, *Environ. Technol.*, 2016, **37**, 369–380.

25 W. Hao, J. Xu, R. Li, X. Zhao, L. Qiu and W. Yang, Developing superhydrophobic rock wool for high-viscosity oil/water separation, *Chem. Eng. J.*, 2019, **368**, 837–846.

26 L. Lin, D. Yu, L. Xu, Y. Huang, M. Huang and H. Kazemian, Enhanced photocatalytic performance and persulfate activation properties by BiOBr supported waste rock wool fibers under LED blue light, *J. Environ. Chem. Eng.*, 2022, **10**, 107963.

27 W. Nie, Q. Tong, Q. Li, W. Yang and W. Hao, From waste to functional materials: a multifunctional electromagnetic interference shielding composite from waste rock wool, *ACS Appl. Electron. Mater.*, 2021, **3**, 2187–2194.

28 Z. Ping, H. Fang, K. Wang, H. Zhang, S. Li, J. Chen and F. Huang, A Universal Cl-PEDOT Coating Strategy Based on Oxidative Chemical Vapor Deposition toward Solar-Driven Multifunctional Energy Management, *Adv. Funct. Mater.*, 2022, **32**, 2208965.

29 Y. Chen, Y. Wang, J. Xu, M. R. Ibn Raihan, B. Guo, G. Yang, M. Li, H. Bao and H. Xu, A 3D Opened Hollow Photothermal Evaporator for Highly Efficient Solar Steam Generation, *Solar RRL*, 2022, **6**, 2200202.

30 Q. Yang, R. Lu, S. Ren, C. Chen, Z. Chen and X. Yang, Three dimensional reduced graphene oxide/ZIF-67 aerogel: effective removal cationic and anionic dyes from water, *Chem. Eng. J.*, 2018, **348**, 202–211.

31 Y. Li, Z. Jin and T. Zhao, Performance of ZIF-67-derived fold polyhedrons for enhanced photocatalytic hydrogen evolution, *Chem. Eng. J.*, 2020, **382**, 123051.

32 J. Wang, Y. Li, S. Xu, C. Lin, X. Ma, Y. Ni and S. Cao, Novel functionalization of ZIF-67 for an efficient broad-spectrum photocatalyst: formaldehyde degradation at room temperature, *New J. Chem.*, 2022, **46**, 2962–2970.

33 D. Fan, Y. Lu, H. Zhang, H. Xu, C. Lu, Y. Tang and X. Yang, Synergy of photocatalysis and photothermal effect in integrated 0D perovskite oxide/2D MXene heterostructures for simultaneous water purification and solar steam generation, *Appl. Catal., B*, 2021, **295**, 120285.

34 T. Zhou, C. Wu, Y. Wang, A. P. Tomsia, M. Li, E. Saiz, S. Fang, R. H. Baughman, L. Jiang and Q. Cheng, Super-tough MXene-functionalized graphene sheets, *Nat. Commun.*, 2020, **11**, 1–11.

35 C. J. Zhang, S. Pinilla, N. McEvoy, C. P. Cullen, B. Anasori, E. Long, S.-H. Park, A. Seral-Ascaso, A. Shmeliov and D. Krishnan, Oxidation stability of colloidal two-dimensional titanium carbides (MXenes), *Chem. Mater.*, 2017, **29**, 4848–4856.

36 J. K. El-Demellawi, S. Lopatin, J. Yin, O. F. Mohammed and H. N. Alshareef, Tunable Multipolar Surface Plasmons in 2D $Ti_3C_2T_x$ MXene Flakes, *ACS Nano*, 2018, **12**, 8485–8493.

37 R. M. Abdelhameed and M. El-Shahat, Fabrication of ZIF-67@ $MIL-125-NH_2$ nanocomposite with enhanced visible light photoreduction activity, *J. Environ. Chem. Eng.*, 2019, **7**, 103194.

38 Y. Cao, Q. Deng, Z. Liu, D. Shen, T. Wang, Q. Huang, S. Du, N. Jiang, C.-T. Lin and J. Yu, Enhanced thermal properties of poly (vinylidene fluoride) composites with ultrathin nanosheets of MXene, *RSC Adv.*, 2017, **7**, 20494–20501.

39 C. E. Shuck, A. Sarycheva, M. Anayee, A. Levitt, Y. Zhu, S. Uzun, V. Balitskiy, V. Zahorodna, O. Gogotsi and Y. Gogotsi, Scalable synthesis of $Ti_3C_2T_x$ mxene, *Adv. Eng. Mater.*, 2020, **22**, 1901241.

40 W. Song, J. Chen, Z. Li and X. Fang, Self-powered MXene/GaN van der Waals heterojunction ultraviolet photodiodes with superhigh efficiency and stable current outputs, *Adv. Mater.*, 2021, **33**, 2101059.

41 L. Ma, T. Zhao, F. Xu, T. You and X. Zhang, A dual utilization strategy of lignosulfonate for MXene asymmetric supercapacitor with high area energy density, *Chem. Eng. J.*, 2021, **405**, 126694.

42 P. Dutta, A. Sikdar, A. Majumdar, M. Borah, N. Padma, S. Ghosh and U. N. Maiti, Graphene aided gelation of MXene with oxidation protected surface for supercapacitor electrodes with excellent gravimetric performance, *Carbon*, 2020, **169**, 225–234.

43 Y. Yue, N. Liu, Y. Ma, S. Wang, W. Liu, C. Luo, H. Zhang, F. Cheng, J. Rao and X. Hu, Highly self-healable3D microsupercapacitor with MXene–graphene composite aerogel, *ACS Nano*, 2018, **12**, 4224–4232.

44 Q. Yang, S. Ren, Q. Zhao, R. Lu, C. Hang, Z. Chen and H. Zheng, Selective separation of methyl orange from water using magnetic ZIF-67 composites, *Chem. Eng. J.*, 2018, **333**, 49–57.

45 S. Sundriyal, V. Shrivastav, H. Kaur, S. Mishra and A. Deep, High-performance symmetrical supercapacitor with a combination of a ZIF-67/rGO composite electrode and a redox additive electrolyte, *ACS Omega*, 2018, **3**, 17348–17358.

46 Y. Zhang, H. Li, S. Liu, N. Wu and S. OuYang, Raman spectroscopic study of irregular network in the process of glass conversion to $CaO–MgO–Al_2O_3–SiO_2$ glass-ceramics, *J. Non-Cryst. Solids*, 2021, **563**, 120701.

47 Y. Gao, M. Leng, Y. Chen, Z. Chen and J. Li, Crystallization products and structural characterization of $CaO–SiO_2$-based mold fluxes with varying Al_2O_3/SiO_2 ratios, *Materials*, 2019, **12**, 206.

48 R. Liu and W. Li, High-thermal-stability and high-thermal-conductivity $Ti_3C_2T_x$ MXene/poly (vinyl alcohol)(PVA) composites, *ACS Omega*, 2018, **3**, 2609–2617.

This journal is © The Royal Society of Chemistry 2023

J. Mater. Chem. A, 2023, **11**, 5296–5308 | **5307**

49 M. Mustakeem, J. K. El-Demellawi, M. Obaid, F. Ming, H. N. Alshareef and N. Ghaffour, MXene-Coated Membranes for Autonomous Solar-Driven Desalination, *ACS Appl. Mater. Interfaces*, 2022, **14**, 5265–5274.

50 A. Sarycheva and Y. Gogotsi, Raman spectroscopy analysis of the structure and surface chemistry of $Ti_3C_2T_x$ MXene, *Chem. Mater.*, 2020, **32**, 3480–3488.

51 D. B. Lioi, G. Neher, J. E. Heckler, T. Back, F. Mehmood, D. Nepal, R. Pachter, R. Vaia and W. J. Kennedy, Electron-Withdrawing Effect of Native Terminal Groups on the Lattice Structure of $Ti_3C_2T_x$ MXenes Studied by Resonance Raman Scattering: Implications for Embedding MXenes in Electronic Composites, *ACS Appl. Nano Mater.*, 2019, **2**, 6087–6091.

52 K.-Y. A. Lin and W.-D. Lee, Self-assembled magnetic graphene supported ZIF-67 as a recoverable and efficient adsorbent for benzotriazole, *Chem. Eng. J.*, 2016, **284**, 888–1027.

53 L. Zhang, A. Wu, M. Tian, Y. Xiao, X. Shi, H. Yan, C. Tian and H. Fu, 2-D porous Ni_3N–Co_3N hybrids derived from ZIF-67/$Ni(OH)_2$ sheets as a magnetically separable catalyst for hydrogenation reactions, *Chem. Commun.*, 2018, **54**, 11088–11091.

54 J. Yan, C. E. Ren, K. Maleski, C. B. Hatter, B. Anasori, P. Urbankowski, A. Sarycheva and Y. Gogotsi, Flexible MXene/graphene films for ultrafast supercapacitors with outstanding volumetric capacitance, *Adv. Funct. Mater.*, 2017, **27**, 1701264.

55 J. Halim, K. M. Cook, M. Naguib, P. Eklund, Y. Gogotsi, J. Rosen and M. W. Barsoum, X-ray photoelectron spectroscopy of select multi-layered transition metal carbides (MXenes), *Appl. Surf. Sci.*, 2016, **362**, 406–417.

56 V. Natu, M. Benchakar, C. Canaff, A. Habrioux, S. Celerier and M. W. Barsoum, A critical analysis of the X-ray photoelectron spectra of $Ti_3C_2T_z$ MXenes, *Matter*, 2021, **4**, 1224–1251.

57 L. Shao, J. Xu, J. Ma, B. Zhai, Y. Li, R. Xu, Z. Ma, G. Zhang, C. Wang and J. Qiu, MXene/RGO composite aerogels with light and high-strength for supercapacitor electrode materials, *Compos. Commun.*, 2020, **19**, 108–113.

58 H. Niu, X. Yang, Q. Wang, X. Jing, K. Cheng, K. Zhu, K. Ye, G. Wang, D. Cao and J. Yan, Electrostatic self-assembly of MXene and edge-rich CoAl layered double hydroxide on molecular-scale with superhigh volumetric performances, *J. Energy Chem.*, 2020, **46**, 105–113.

59 R. Xu, N. Wei, Z. Li, X. Song, Q. Li, K. Sun, E. Yang, L. Gong, Y. Sui and J. Tian, Construction of hierarchical 2D/2D Ti_3C_2/MoS_2 nanocomposites for high-efficiency solar steam generation, *J. Colloid Interface Sci.*, 2021, **584**, 125–133.

60 C. Hu, J. Xu, Y. Wang, M. Wei, Z. Lu and C. Cao, Core–shell crystalline ZIF-67@ amorphous ZIF for high-performance supercapacitors, *J. Mater. Sci.*, 2020, **55**, 16360–16373.

61 T. Sun, S. Hao, R. Fan, M. Qin, W. Chen, P. Wang and Y. Yang, Hydrophobicity-Adjustable MOF Constructs Superhydrophobic MOF-rGO Aerogel for Efficient Oil–Water Separation, *ACS Appl. Mater. Interfaces*, 2020, **12**, 56435–56444.

62 X. Wu, T. Gao, C. Han, J. Xu, G. Owens and H. Xu, A photothermal reservoir for highly efficient solar steam generation without bulk water, *Sci. Bull.*, 2019, **64**, 1625–1633.

63 Y. Xu, X. Xiao, X. Fan, Y. Yang, C. Song, Y. Fan and Y. Liu, Low cost, facile, environmentally friendly all biomass-based squid ink-starch hydrogel for efficient solar-steam generation, *J. Mater. Chem. A*, 2020, **8**, 24108–24116.

64 C. Song, M. S. Irshad, Y. Jin, J. Hu and W. Liu, Arabic-dome-inspired hierarchical design for stable and high-efficiency solar-driven seawater desalination, *Desalination*, 2022, **544**, 116125.

65 J. Xiong, J. Yi, S. Peng, Z. Yang, Y. Wu, W. Wang, S. Lv, J. Peng, C. Xue and X. Min, Plant transpiration-inspired environmental energy-enhanced solar evaporator fabricated by polypyrrole decorated polyester fiber bundles for efficient water purification, *J. Clean. Prod.*, 2022, **379**, 134683.

66 H. Liu, M. K. Alam, M. He, Y. Liu, L. Wang, X. Qin and J. Yu, Sustainable cellulose aerogel from waste cotton fabric for high-performance solar steam generation, *ACS Appl. Mater. Interfaces*, 2021, **13**, 49860–49867.

67 Z. Xie, J. Zhu and L. Zhang, Three-dimensionally structured polypyrrole-coated setaria viridis spike composites for efficient solar steam generation, *ACS Appl. Mater. Interfaces*, 2021, **13**, 9027–9035.

68 G. Zhao, Y. Chen, L. Pan, B. Chen, L. Ren, X. Xiao, H. Yang and W. Xu, Plant-inspired design from carbon fiber toward high-performance salt-resistant solar interfacial evaporation, *Sol. Energy*, 2022, **233**, 134–141.

69 F. Meng, Z. Ding, Z. Chen, K. Wang, X. Liu, J. Li, T. Lu, X. Xu and L. Pan, N-doped carbon@Cu core–shell nanostructure with nearly full solar spectrum absorption and enhanced solar evaporation efficiency, *J. Mater. Chem. A*, 2022, **10**, 9575–9581.

70 P.-F. Liu, L. Miao, Z. Deng, J. Zhou, Y. Gu, S. Chen, H. Cai, L. Sun and S. Tanemura, Flame-treated and fast-assembled foam system for direct solar steam generation and non-plugging high salinity desalination with self-cleaning effect, *Appl. Energy*, 2019, **241**, 652–659.

71 Y. Lu, D. Fan, Z. Shen, H. Zhang, H. Xu and X. Yang, Design and performance boostof a MOF-functionalized-wood solar evaporator through tuning the hydrogen-bonding interactions, *Nano Energy*, 2022, **95**, 107016.

72 Y. Kuang, C. Chen, S. He, E. M. Hitz, Y. Wang, W. Gan, R. Mi and L. Hu, A high-performance self-regenerating solar evaporator for continuous water desalination, *Adv. Mater.*, 2019, **31**, 1900498.

73 Y. Wang, X. Wu, P. Wu, H. Yu, J. Zhao, X. Yang, Q. Li, Z. Zhang, D. Zhang and G. Owens, Salt isolation from waste brine enabled by interfacial solar evaporation with zero liquid discharge, *J. Mater. Chem. A*, 2022, **10**, 14470–14478.

74 T. Gao, Y. Wang, X. Wu, P. Wu, X. Yang, Q. Li, Z. Zhang, D. Zhang, G. Owens and H. Xu, More from less: improving solar steam generation by selectively removing a portion of evaporation surface, *Sci. Bull.*, 2022, **67**, 1572–1580.

5308 | *J. Mater. Chem. A*, 2023, **11**, 5296–5308

This journal is © The Royal Society of Chemistry 2023